

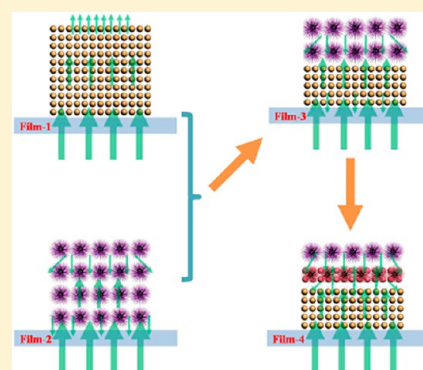
Tripartite Layered Photoanode from Hierarchical Anatase TiO₂ Urchin-Like Spheres and P25: A Candidate for Enhanced Efficiency Dye Sensitized Solar Cells

Pengfei Cheng, Sisi Du, Yaxin Cai, Fengmin Liu,* Peng Sun, Jie Zheng, and Geyu Lu*

State Key Laboratory on Integrated Optoelectronics Jilin University Region; College of Electronic Science and Engineering, Jilin University, 2699 Qianjin Street, Changchun 130012, P. R. China

S Supporting Information

ABSTRACT: A trilaminar layer photoanode for dye-sensitized solar cells (DSSCs) was constructed using urchin-like TiO₂ hierarchical microspheres and P25. The top layer made of hierarchical microspheres enhanced light scattering; the middle layer consisting of P25 and as-prepared microspheres is a multifunctional layer for DSSCs, high adsorption ability to the dye, light scattering ability, and slow recombination rates coexistence; the bottom layer used P25. The DSSCs based on the photoanode with tripartite-layers structure exhibited a much higher short-circuit photocurrent density of 18.97 mA cm⁻² and energy conversion efficiency of 8.80%, which indicated a 36% increase in the conversion efficiency compared to those of the P25 electrode (14.51 mA cm⁻², 6.50%). The great improvements of photocurrent density and energy conversion efficiency for hierarchical TiO₂ microspheres were mainly attributed to a considerable surface area, a higher light scattering ability, and slower electron recombination rates for the former.



INTRODUCTION

Since the pioneering paper about dye-sensitized solar cells (DSSCs) was published by O'Regan and Grätzel in 1991, DSSCs, as a new generation photovoltaic device, have been studied extensively^{1–5} because of their high efficiency and low-cost. It is well-known that DSSCs can perform relatively better compared with other solar cell technologies even under diffuse light conditions and at high temperatures. DSSCs offer the possibilities to design solar cells with large shapes, color, and transparency. Based on these factors, integration into different products opens up new commercial opportunities. Currently, in order to enhance the performance of the DSSCs, much effort has been devoted to the development of high performance of DSSCs. In general, high specific surface area, fast electron transport, and pronounced light-scattering effects are indispensable to a high performance photoanode. Therefore, DSSCs have made significant achievements by using TiO₂ photoelectrodes with various TiO₂ morphologies such as nanoparticles,^{6–8} mesoporous beads,^{9–13} and nanorods and nanotubes.^{14–18} Moreover, the structure of the photoanode plays an important role in enhancing the performance of cells. So far, the highest power conversion efficiency of over 12% has been achieved by using a porphyrin-based-dye light harvester, a volatile organic solvent electrolyte with cobalt (II/III), and a double layer TiO₂ photoelectrode consisting of dye adsorption by a transparent TiO₂ film layer (20 nm sized TiO₂ nanoparticle) and top particle light scattering layer (large particle size, 400 nm).¹⁹ This shows that the light scattering layer plays a key role in enhancing the performance of the DSSCs. In the DSSCs, the light scattering layer can increase the

optical path length which irradiate into the TiO₂ film. Although the large particles with flat surfaces possess excellent light scattering properties, they are not suitable as photoanode materials because of less dye loading ascribed from the much lower surface area. Therefore, the rough surface or hierarchically structured photoanode materials are more suitable for DSSCs and exhibit enhanced power conversion efficiency owing to their superior dye adsorption properties.^{20–22} Moreover, recent bifunctional hierarchically structured materials (TiO₂,^{11,23} ZnO,^{24,25} and SnO₂^{26,27}) consisting of nanoparticles have been widely investigated as photoanodes for DSSCs and exhibited enhanced power conversion efficiency owing to their superior dye-adsorption properties and light-scattering abilities.

In this work, we developed a one-step hydrothermal method to directly convert commercial P25 powders into monodisperse anatase TiO₂ with 3D urchin-like structures with an average diameter of about 2 μm. This novelty structure was built from single-crystalline nanothorns. Moreover, nitrogen adsorption isotherm analysis demonstrated that the obtained hierarchical TiO₂ microspheres had an extraordinary specific surface area. These hierarchical TiO₂ microspheres were ideal for constructing porous photoanode films due to the high specific surface area. Indeed, DSSCs based on as-prepared product have achieved much improved efficiency compared to cells fabricated with a standard P25 TiO₂ photoanode.

Received: July 11, 2013

Revised: October 25, 2013

Published: October 28, 2013

EXPERIMENTAL SECTION

Synthesis of Materials. The TiO₂ microspheres (designated as TMS) were prepared by a one step hydrothermal process. In a typical process, 0.1 g of P25 (Degussa) was added to 60 mL of 10 M NaOH solution. After ultrasonication and stirring for 5 min alternately, the mixture was injected into a 100 mL Teflon-lined autoclave. A total of 8 mL of hydrogen peroxide (30%) was then added into the mixture under stirring. After the mixture was stirred for 5 min, the autoclave was sealed and heated at 160 °C for 2 h. The system was then allowed to cool to ambient temperature. The as-obtained white product was collected by centrifuge, washed with 0.2 M HCl solution three times, and then centrifuged and washed with deionized water three times to remove any possible ionic remains. Finally, the products were dried at 60 °C, calcined at 450 °C for 2 h with a heating rate of 10 °C min⁻¹ in air, and collected for further characterization.

Characterization of Materials. The crystal structure of the as-prepared product was investigated by X-ray diffraction (XRD; Rigaku TTRIII, with Cu K α 1 radiation). The morphology and microstructure were examined by field-emission scanning electron microscopy (FESEM, JEOL JSM-7500F, operated at an acceleration voltage of 15 kV). Transmission electron microscopy (TEM) measurements were obtained on a JEOL JEM-2100 microscope operated at 200 kV. The specific surface area was measured using the Brunauer–Emmett–Teller (BET) equation based on the nitrogen adsorption isotherm obtained with a Micromeritics Gemini VII apparatus (Surface Area and Porosity System).

Fabrication of the DSSCs. To prepare the DSSC working electrodes, 0.3 g of TMS was added into the mixture of 5 mL of ethylalcohol and 1 g of terpinol and treated with an ultrasonic bath for 60 min to form a paste. First, a thick film of the P25 nanocrystalline (~25 nm, surface area: 56 m²g⁻¹, Degussa) was formed on fluorine-doped tin oxide (FTO) glass (resistivity 14 Ω /square, Nippon Sheet Glass, Japan) by doctor blade technique. After drying at 125 °C for 6 min, the TMS layer was deposited on the P25 thick films by the same process; the thick film with double-layer structure was allowed to dry in 125 °C before sintering at various temperatures of 325–500 °C in air. Then, the thick film with double-layer structure was loaded with dye by immersing it in a 0.4 mM Ru-dye (*cis*-dithiocyanate-*N,N'*-bis(4-carboxylate-4 tetrabutyl ammonium-carboxylate-2,2'-bipyridine) ruthenium(II) (known as N719, Solaronix) for 24 h at room temperature. The resulting photoanode using a double layer structure was combined with the Pt-sputtered FTO counter electrode, acetonitrile/valeronitrile (85/15v/v) electrolyte containing 0.6 M 1,2-dimethyl-3-propylimidazolium iodide, 0.03 M I₂, 0.1 M guanidinium thiocyanate, and 0.5 M 4-tert-butylpyridine (Aldrich) for making a DSSC by a vacuum filling method. The working electrode film area for the solar cell performance test was representatively 0.25 cm².

Measurements of DSSCs' Performance. The current–voltage (*I*–*V*) characteristics were measured by using a Keithley 2400 Source Meter under under one sun AM 1.5 G (100 mW cm⁻²) illumination with a solar light simulator (Newport, model: 94023A). A 450 W xenon arc lamp (Newport, model: 6280NS) served as a light source, and its incident light intensity was calibrated with a NREL-calibrated Si solar cell equipped with an optical filter to approximate AM 1.5 G one sun light intensity before each measurement. The

incident photon to current efficiency (IPCE) spectra was measured as a function of wavelength from 350 to 800 nm with a spectral resolution of 5 nm on the basis of a Spectral Product Zolix DSC300PA. Diffuse-reflectance spectra were measured on the same film samples on a Perkin-Elmer UV/vis spectrophotometer (SHIMADZU 2550). The EIS experiments were performed using an electrochemical workstation (Solartron SI1287) at a bias potential of –0.8 V. Intensity-modulated photovoltage spectroscopy (IMVS) and intensity-modulated photocurrent spectroscopy (IMPS) measurements were carried out on a electron lifetime and dispersion test system (PSL-100) with a diode laser light source with variable intensities at 620 nm.

RESULTS AND DISCUSSION

Characterization of Materials. The structure and morphology of the TiO₂ microsphere (TMS) samples were observed by scanning electron microscopy (SEM) and transmission electron microscopy (TEM). Figure 1a displays

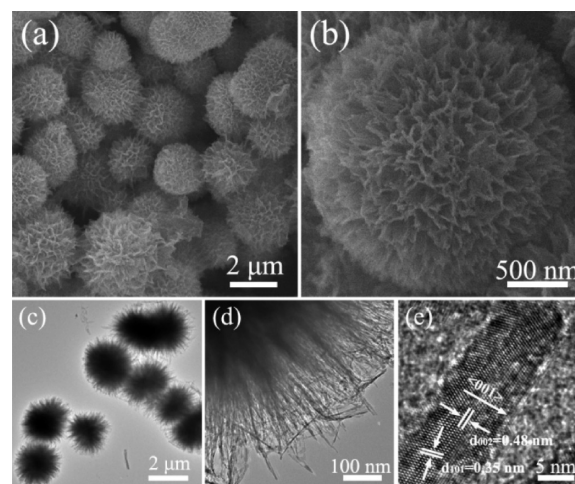


Figure 1. (a and b) SEM images of the urchin-like TiO₂ hierarchical microspheres with different magnifications and (c and d) TEM and (e) HRTEM images of as prepared TiO₂ nanourchin.

the SEM image of the as-prepared sample. It can be seen that the TiO₂ microspheres are monodisperse and the diameter range of spheres is from 1.5 to 2.5 μ m. A higher magnification SEM image shown in Figure 1b reveals obviously that the microspheres are composed of serried thorns, from a lot of plicated ribbon. Panels c and d in Figure 1 are the TEM images of the as-prepared samples, where the thorn structure is further exhibiting. Furthermore, the HRTEM image of an individual thorn indicates a highly crystallized anatase phase structure. The interplane spacings of 0.48 and 0.35 nm imply that the thorn is growing along the {001} direction and enclosed with the {101} facets (Figure 1e).

The X-ray diffraction (XRD) pattern of the sample prepared by the hydrothermal method is shown in Figure 2a. The well-defined and sharp Bragg peaks with high intensity indicate good crystallinity of the sample. As can be seen from the XRD pattern, the 2θ values at 25.28, 37.80, 48.05, 53.89, 55.06, 62.69, 68.76, 70.31, and 75.03° can be assigned to (101), (004), (200), (105), (211), (204), (116), (220), and (215) crystal planes of anatase TiO₂ respectively. All identified peaks can be perfectly indexed to anatase TiO₂ (JCPDS card no. 21-1272). Meanwhile, the average crystallite sizes of the TiO₂ samples

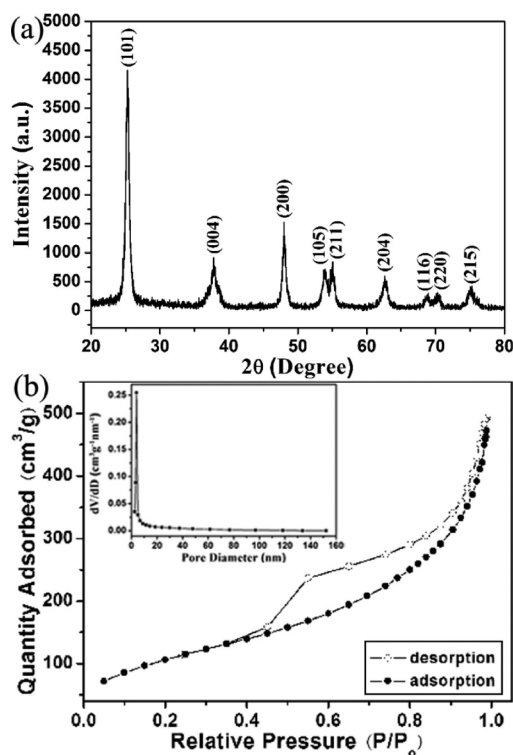


Figure 2. (a) XRD patterns of the as-synthesized urchin-like TiO_2 hierarchical microspheres. (b) Nitrogen sorption isotherms of the as-prepared nanourchin. The inset shows the pore size distributions calculated using the BJH method.

were calculated using the Scherrer formula: $D = K\lambda/\beta \cos \theta$, where λ was the wavelength of the X-ray radiation ($\lambda = 0.15418$ nm), K was the Scherrer constant ($K = 0.89$), θ was the position of X-ray diffraction peak, and β was the full width at half-maximum (fwhm) of the (101) plane for anatase TiO_2 . The calculated size is about 13.5 nm, indicating that the thickness of each layer venation is thin and sparse. This is consistent with the information of SEM and TEM above, the nitrogen adsorption–desorption isotherm, and pore size distribution (inset) of nanourchin.

The adsorption–desorption isotherms are typical type IV with a sharp capillary condensation step at high relative pressures ($P/P_0 = 0.575$) and H1 hysteresis loop according to the IUPAC classification, indicating that the materials contain disordered mesopores (Figure 2b).²⁸ Pore size distribution curves were calculated from the desorption branch of a nitrogen isotherm by the BJH method using the Halsey equation. The pore size distribution curve revealed a correspondingly narrow pore size distribution (5–40 nm) with a peak size of about 4 nm (the inset of Figure 2b).²⁹ Moreover, The BET surface area of the products was calculated to be $392 \text{ m}^2 \text{ g}^{-1}$ by the Brunauer–Emmett–Teller (BET) method.

Photovoltaic Performances. The novel anatase TiO_2 microspheres (TMS) are further used as a photoanode in DSSCs. For comparison, four kinds of films (film 1, P25; film 2, TMS; film 3, P25 + TMS; film 4, P25 + hybrid P25 and TMS + TMS) with similar thicknesses were screen printed onto the FTO glass with a pre-coated TiO_2 compact layer.³⁰ The cross-sectional SEM images (shown in Figure 3) clearly show films 1, 2, 3, and 4 with around $15 \mu\text{m}$ thick P25 nanoparticles, $15 \mu\text{m}$ thick TMS, $7.5 \mu\text{m}$ P25 + $7.5 \mu\text{m}$ TMS, $7.5 \mu\text{m}$ thick P25 + $4 \mu\text{m}$ hybrid P25 and TMS + $3.5 \mu\text{m}$ TMS, respectively. The

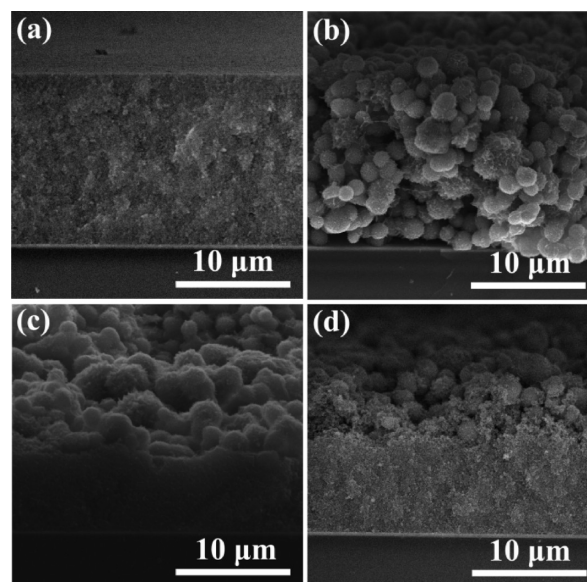


Figure 3. SEM images of the four TiO_2 films on compact layer/FTO glass. Cross-section images of films 1 (a), 2 (b), 3 (c), and 4 (d).

active layer (P25 or scattering layer) is mainly controlled by the same thickness and same conditions. For film 4, a hybrid top-layer composed of TMS and P25 with 1:1 weight ratio was utilized. The schematic structure diagram of film 4 is shown in Figure 4 (inset).

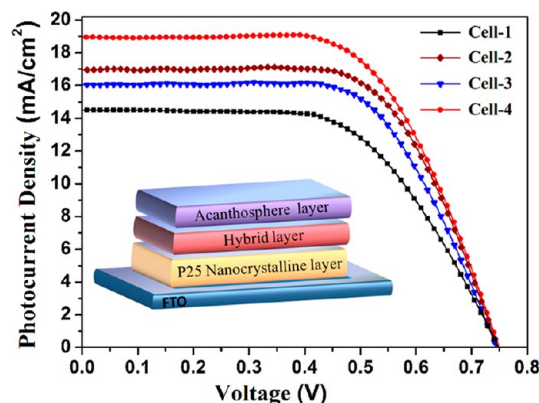


Figure 4. I – V curves of the DSSCs based on different photoanodes measured under one sun illumination (AM 1.5 G, 100 mW cm^{-2}). ■, cell 1; ▼, cell 2; ◆, cell 3; and ●, cell 4. The inset displays the structure of film 4.

Under illumination of AM 1.5 simulated sunlight with a power density of 100 mW/cm^2 , the photocurrent density–photovoltage (J – V) curves of DSSCs based on the four films (cell 1, film 1; cell 2, film 2; cell 3, film 3; and cell 4, film 4) are shown in Figure 4, and the corresponding photovoltaic parameters are summarized in Table 1. As shown in Figure 4 and Table 1, the fill factor (FF) and open-circuit photovoltage (V_{oc}) varied little among the four cells, the variation of the energy conversion efficiency (η) mainly came from the change in the short-circuit photocurrent density (J_{sc}). The short-circuit current density (J_{sc}) increases from 14.51 to 16.05 to 16.96 to 18.97 mA/cm^2 as the film varied from 1 to 2 to 3 to 4, leading to the power conversion efficiency (η) improving from 6.50 to 7.52 to 8.09 to 8.80% . It is noteworthy that the most efficient

Table 1. Photovoltaic Data of Four Different TiO₂ Film Structures, Measured under AM 1.5 G One Sun Illumination (100 mW cm⁻²) and Simulative Value of Resistance (R_s , R_1 , and R_2) from EIS Spectra Calculated by Equivalent Circuit As Shown in Figure 7^a

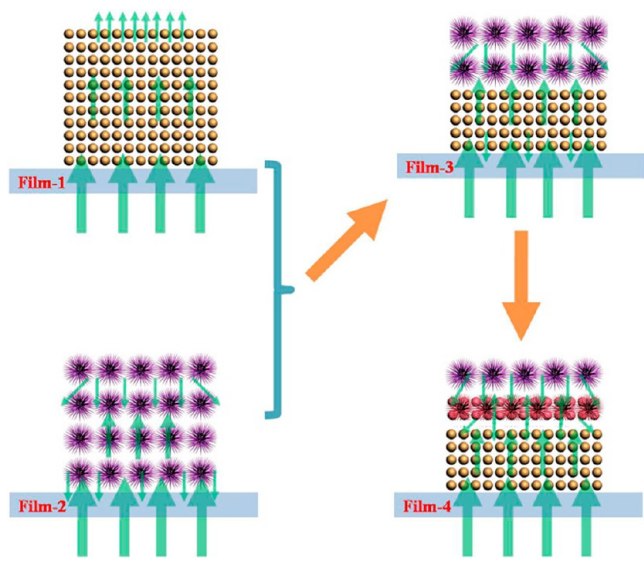
| sample | J_{sc} (mA/cm ²) | V_{oc} (mV) | FF (%) | η (%) | R_s (Ω) | R_1 (Ω) | R_2 (Ω) | dye adsorbed ($\times 10^{-7}$ mol/cm ²) |
|--------|--------------------------------|---------------|--------|------------|--------------------|--------------------|--------------------|---|
| cell 1 | 14.51 | 747 | 0.60 | 6.50 | 16.7 | 9.9 | 61.0 | 0.96 |
| cell 2 | 16.05 | 744 | 0.63 | 7.52 | 16.6 | 9.7 | 69.8 | 2.12 |
| cell 3 | 16.96 | 745 | 0.64 | 8.09 | 16.8 | 9.4 | 138.8 | 1.81 |
| cell 4 | 18.97 | 749 | 0.62 | 8.80 | 16.6 | 9.5 | 169.2 | 2.02 |

^a J_{sc} short-circuit photocurrent density. V_{oc} open-circuit photovoltage. η , total power conversion efficiency. FF, fill factor. From I - V measurements and UV-vis adsorption.

photovoltaic performance of 8.80% is achieved for cell 4 with P25 + hybrid P25 and TMS + TMS film (film 4 shown as Figure 4 inset), exhibiting 18.97 mA/cm² in J_{sc} , 749 mV in V_{oc} and 0.62 in FF. Furthermore, both the J_{sc} and η of the DSSCs based on film 4 improve by 31% and 36%, respectively, compared to those of films 1 (P25), 3, and 4 having the same thickness of P25 to conclude the conversion efficiency can be enhanced by tripartite layered structure, which will be discussed later in detail.

It is well-known that the TiO₂ photoanode is a carrier of the dye, and the dye is a harvester of the photon; the photocurrent is strongly related to the light-harvesting capability of TiO₂ photoanode.³¹ Therefore, to promote dye loading and light scattering of the electrodes are two equally important tasks for light-harvesting. The schematic diagrams of four film structures and incident light analog path is shown in Scheme 1. The P25

Scheme 1. Schematic Diagrams of Four Film Structures and the Incident Light Analog Path



has a high transparency for incident light due to its small size (film 1), and TiO₂ microspheres (TMS) contained films (films 2, 3, and 4) reveal a high diffuse reflection. Compared to films 2 and 3, film 4 has a higher utilization of the incident light, and the schematic diagram indicates that such an ingenious film structure can give a plus contribution to the highest J_{sc} . Moreover, the combination between the P25 and TMS can improve the transport property and increase the recombination resistance of the photoelectrons (UV-vis reflectance spectra and impedance spectroscopy will be given later). Moreover, because of the excellent specific surface area photoanode

materials that lead to high dye adsorption amount and a TMS with a surface area of 392 m² g⁻¹, it is a surprising surface area for photoanode materials. The amounts of N719 dye adsorbed on these four films were investigated by thorough desorption in 1 mM NaOH solution and then obtained by measuring the UV-vis absorption spectra of the solutions. The dye loading of cells 2, 3 and 4 (contain the TMS) are 2.2, 1.9, and 2.1 times higher than that of cell 1 (see Table 1), respectively. The higher dye loading of cells 2, 3, and 4 are ascribed to the larger specific surface area of the film.

Hierarchical spheres with submicrometer size consisting of nanoparticles have been proven to enhance the light scattering effect, leading to higher photocurrent and photovoltaic performance. When the size of the particle is larger than the optical wavelength, the scattering is mainly caused by diffraction within a small angle range which is produced in back of the particle; this scattering is called diffraction scattering. When the particle is large, the incident light through multiple reflection and refraction of the scatterer (photoanode material), the effect of geometrical optics is increasing, and the light spread in all directions. According to the nature of diffraction, the larger the scatterer, the closer to the center for diffracted light. Therefore, for large scattering particles (micrometer level), the role of geometrical optics is significant, the scattering light is mainly formed from the diffraction effect. The incorporation of large nanoparticles has been employed for use as light-scattering centers to increase the optical length in the film, and an enhanced light-harvesting has been demonstrated both experimentally^{32,33} and theoretically.³⁴ Especially, TMS with a rough surface can scatter the light which irradiated into the film effectively.

To further investigate the light scattering property of the TMS material and P25 base on the four films,^{35,36} the UV-vis reflectivity spectra of each film was studied. Figure 5 shows the UV-vis reflectance spectra of the four films with and without dye loading. Before the dye adsorption, both TMS contained film (film 2, 3, 4) and the P25 (film 1) film had high reflectivity in the wavelength range of 400–500 nm. However, the reflectivity of the P25 film (film 1) decreased rapidly over 500 nm while the TMS contained films (films 2, 3, and 4) still kept quite high reflectivity in the same range, indicating the TMS in the films has a better light-scattering ability than that in the P25 film due to the comparable sphere size to the wavelength of visible.³⁷ After dye adsorption, the reflectance of film 4 decreases drastically from ca. 50% to ca. 20% in the short wavelength ranging from 400 to 600 nm (Figure 5b), which is mainly attributed to light absorption by the dye molecules. In the long wavelength region, the dye-absorbed film 4 still retained a substantially higher reflectance than the dye-absorbed film 1, which further supports our argument that the higher J_{sc} for cell 4 compared to cell 1 is a consequence of

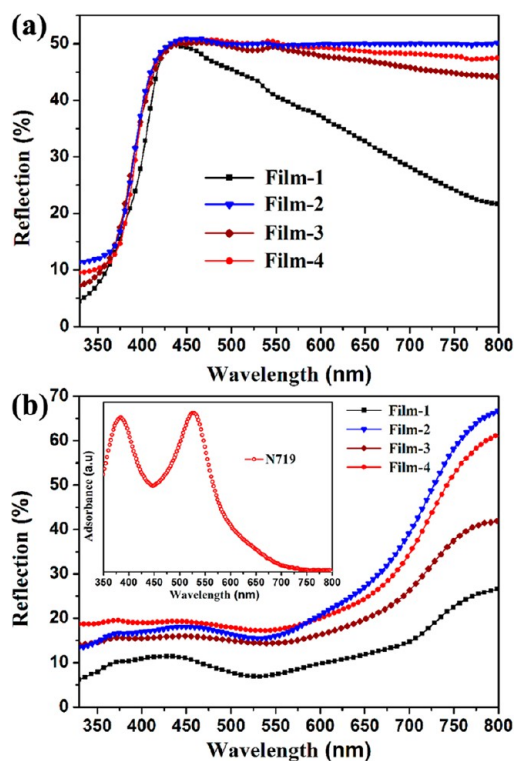


Figure 5. UV–vis reflection of four films without (a) and with (b) N719 dye loading. The inset in panel b gives the UV–vis absorption spectrum of N719. ■, film 1; ▼, film 2; ◆, film 3; and ●, film 4.

the better light scattering property of the acanthosphere structure. However, the difference of the two samples in light scattering efficiency may not be proportional to the difference in IPCE since the IPCE can be affected by a number of parameters.³⁸

Figure 6 shows incident photon to current efficiency (IPCE) spectra for the four DSSCs; the IPCE spectra of the DSSCs

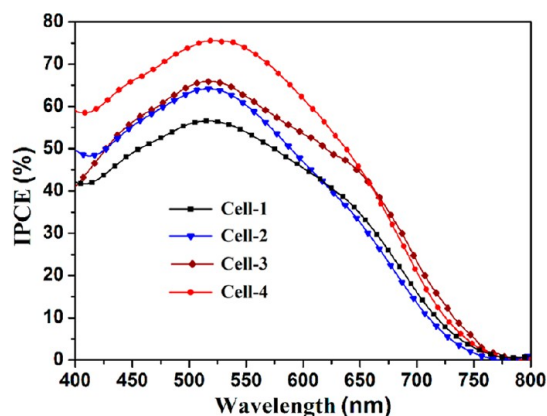


Figure 6. Incident photon to current conversion efficiency (IPCE) curves of the TiO₂ electrodes prepared from four TiO₂ samples. ■, cell 1; ▼, cell 2; ◆, cell 3; and ●, cell 4.

using four kinds of photoanodes and same dye (N719) display maxima at same wavelength (about 525 nm). Cell 4 possesses the highest IPCE values over most of the spectral region (400–660 nm), while in the long wavelength region (660–750 nm) slightly lower than cell 3, it probably arose from the prominent light-scattering effect of film 3 as seen in Figure 5a,b. Though

the scattering ability of film 4 reveals slightly lower than film 3, both films 3 and 4 in terms of scattering ability is very excellent. From what has been discussed above, cell 4 had the highest energy conversion efficiency as seen in Table 1. More reasons for the energy conversion efficiency of cell 4 higher than cell 3 will be further discussed.

To further shed light on the difference in V_{oc} , the electrochemical impedance spectroscopy (EIS) of these four DSSCs based on different photoanode structures were measured in the dark under a forward bias of -0.8 V.^{39,40} As shown in Figure 7, two semicircles were observed in the

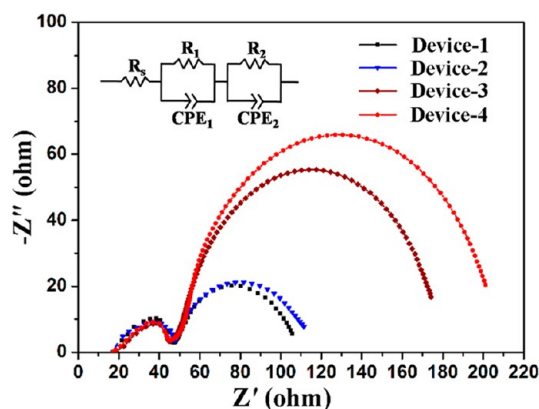


Figure 7. Nyquist plots from electrochemical impedance spectra of the four films together measured in the dark at -0.8 V bias. The inset illustrates the equivalent circuit simulated to fit the impedance spectrum.

Nyquist plots. The smaller and larger semicircles in the Nyquist plots are attributed to the charge transfer at the counter electrode/electrolyte interface and the TiO₂/dye/electrolyte interface, respectively. The sheet resistance (R_s) of substrate, charge transfer resistance of the counter electrode (R_1), and recombination resistance (R_2) were analyzed by Z-view software using an equivalent circuit containing a constant phase element (CPE) and resistances (R ; Figure 7, inset).⁴¹ As shown in Figure 7 and depicted in Table 1, the cells based on these four photoanode structure devices reveal similar R_s and R_1 values of 16.7 ± 0.1 and $9.7 \pm 0.3 \Omega$, respectively, due to the use of the same counter electrode (Pt/FTO glass) and electrolyte. However, the recombination resistance (R_2) of cell 4 (169.2Ω) is larger than that of other cells (61.0 , 69.8 , and 138.8Ω). This is in agreement with the large specific surface area of the hierarchical TiO₂ structure with appropriate size, and the ingenious tripartite layers of photoanode structure reveals a larger electron transfer rate.

After carefully analyzing and fitting the EIS results, we resorted to intensity modulated photocurrent/photovoltage spectroscopy (IMPS/IMVS).^{42–44} In these studies, we used a diode laser light source with variable intensities at 620 nm. Figure 8 represents the main results in the form of the electron diffusion coefficient (D_n) and electron lifetime (τ_e) as a function of open-circuit voltage (V_{oc}) for these four DSSCs based on different photoanode structures. Clearly recognized are the power law dependences of the electron diffusion coefficient (D_n) and τ_e on V_{oc} , which are in accordance with the well-known trapping–detrapping model customarily used to describe electron transport/recombination in DSSCs.⁴⁵ On the whole, the small variation of the slopes of the four cells is commonly thought to arise from the different backbones and

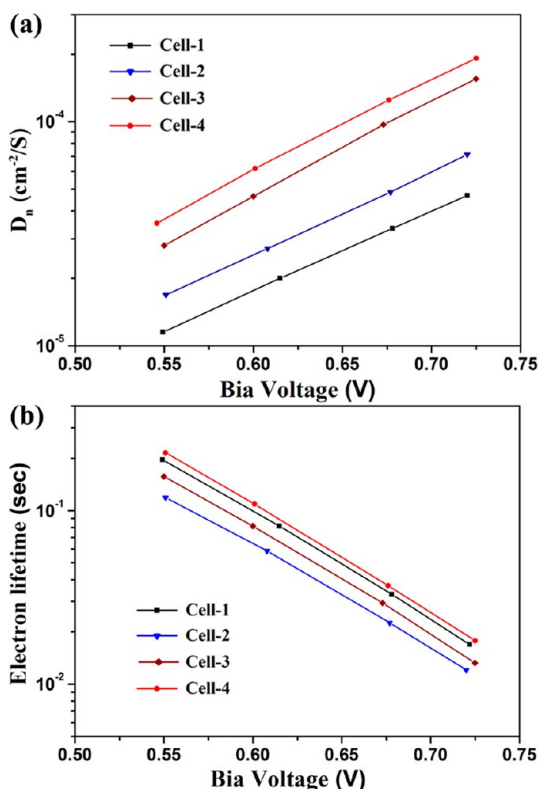


Figure 8. (a) Electron diffusion coefficients and (b) electron lifetimes as a function of the short-circuit currents for the four DSSCs. \blacksquare , cell 1; \blacktriangledown , cell 2; \blacklozenge , cell 3; and \bullet , cell 4.

porosities of the corresponding photoanode films. Notably, whereas τ_r appears to be insensitive to the morphology of our photoanode films, D_n depends very much on the morphology.

Figure 8a displays the D_n curve of the TMS-derived DSSC that still lies above that of the P25-derived DSSC. Specially, the curve of cell 4 (a tripartite layered photoanode) lies the highest, indicating faster electron transport of the former than that of the latter. This can be accounted for by the high crystallinity and uniformity of the TMS already divulged above by XRD and TEM, which would boost both the interior conductivity and interfacial conductivity though the (101) planar contacts between nanocrystals. This significant improvement of electron transport can be understood by invoking two basic causes. The first is related to the close packing between the microspheres, resulting in the very good interior contacts between the constituent nanoparticles. The second is our success in the unique structure of photoanode, as illustrated by Figure 3d, which builds a sort of highway to facilitate electron transport.

Next, we move on to discussing the lifetime or recombination time (τ_r) in the four DSSCs (Figure 8b).⁴⁶ As expected, cell 4 possesses the highest τ_r values due to its ingenious tripartite layers. However, the τ_r of electrons with I_3^- ions in cell 1 is slightly higher than those in cells 2 and 3. Extrapolating to the high J_{sc} region, the τ_r curves of the TMS-contained films would lie above that of the P25 film. This result is presumably ascribable to more defects in films 2 and 3 than in film 1 (P25) but much larger specific surface areas of the TMS-derived films (films 2, 3, and 4), which allow larger amounts of dye molecule loading than that of the P25 (see Table 1). The slightly decreased τ_r has not yet toppled the performance of cells 2 and 3 as a whole.

CONCLUSIONS

A trilaminar layer photoanode for dye-sensitized solar cells (DSSCs) was constructed using urchin-like TiO_2 hierarchical microspheres and P25, and the middle layer consisting of P25 and as-prepared microspheres is a multifunctional layer for DSSCs, high adsorption ability to the dye, light scattering ability, and slow recombination rates coexistence. The DSSCs based on the photoanode with a tripartite-layers structure exhibited a much higher short-circuit photocurrent density of 18.97 mA cm^{-2} and energy conversion efficiency of 8.80%, which indicated a 36% increase in the conversion efficiency compared to those of P25 electrode (14.51 mA cm^{-2} , 6.50%), and the great improvements of photocurrent density and energy conversion efficiency for hierarchical TiO_2 microspheres were mainly attributed to a considerable surface area, a higher light scattering ability, and slower electron recombination rates for the former.

ASSOCIATED CONTENT

Supporting Information

Additional discussion on dark current potential scans, including a figure and references. This material is available free of charge via the Internet at <http://pubs.acs.org>.

AUTHOR INFORMATION

Corresponding Author

*Fax: +86 431 85167808. Tel: +86 431 85167808. E-mail: lgy@jlu.edu.cn, liufm@jlu.edu.cn.

Notes

The authors declare no competing financial interest.

ACKNOWLEDGMENTS

This work is supported by the National Nature Science Foundation of China (Nos. 61074172, 61134010, 60906036, and 61377058), Program for Chang Jiang Scholars and Innovative Research Team in University (No. IRT1017), and "863" High Technology Project (2013AA030902).

REFERENCES

- (1) Hara, K.; Kurashige, M.; Dan-Oh, Y.; Kasada, C.; Shinpo, A.; Suga, S.; Sayama, K.; Arakawa, H. Design of new coumarin dyes having thiophene moieties for highly efficient organic-dye-sensitized solar cells. *New J. Chem.* **2003**, *27*, 783–785.
- (2) Wang, Z. S.; Li, Y. F.; Huang, C. H.; Wang, L.; Wei, M.; Jin, L. P.; Li, N. Q. Photoelectric Conversion Properties of Nanocrystalline TiO_2 Electrodes Sensitized with Hemicyanine Derivatives. *J. Phys. Chem. B* **2000**, *104*, 9676–9682.
- (3) Islam, A.; Sugihara, H.; Yanagida, M.; Hara, K.; Katoh, R.; Murata, S.; Arakawa, H. Efficient panchromatic sensitization of nanocrystalline TiO_2 films by β -diketonato ruthenium polypyridyl complexes. *New J. Chem.* **2002**, *26*, 966–968.
- (4) Zabri, H.; Gillaizeau, I.; Bignozzi, C. A.; Caramori, S.; Charlot, M. F.; Cano-Boquera, J.; Odobel, F. Synthesis and comprehensive characterizations of new cis-Ru(L)(2)X(2) (X = Cl, CN, and NCS) sensitizers for nanocrystalline TiO_2 solar cell using Bis-phosphonated bipyridine ligands (L). *Inorg. Chem.* **2003**, *42*, 6655–6666.
- (5) Wang, Z. S.; Li, F. Y.; Huang, C. H. Photocurrent Enhancement of Hemicyanine Dyes Containing RSO_3^- Group through Treating TiO_2 Films with Hydrochloric Acid. *J. Phys. Chem. B* **2001**, *105*, 9210–9217.
- (6) Grätzel, M. Solar energy conversion by dye-sensitized photo-voltaic cells. *Inorg. Chem.* **2005**, *44*, 6841–6851.
- (7) Chou, T. P.; Zhang, Q. F.; Russo, B.; Fryxell, G. E.; Cao, G. Z. Titania particle size effect on the overall performance of dye-sensitized solar cells. *J. Phys. Chem. C* **2007**, *111*, 6296–6302.

- (8) Wu, X.; Chen, Z. G.; Lu, G. Q.; Wang, L. Z. Nanosized Anatase TiO₂ Single Crystals with Tunable Exposed (001) Facets for Enhanced Energy Conversion Efficiency of Dye-Sensitized Solar Cells. *Adv. Funct. Mater.* **2011**, *21*, 4167–4172.
- (9) Kim, Y. J.; Lee, M. H.; Kim, H. J.; Lim, G.; Choi, Y. S.; Park, N. G.; Kim, K.; Lee, W. Formation of Highly Efficient Dye-Sensitized Solar Cells by Hierarchical Pore Generation with Nanoporous TiO₂ Spheres. *Adv. Mater.* **2009**, *21*, 3668–3673.
- (10) Chen, D. H.; Huang, F. Z.; Cheng, Y. B.; Caruso, R. A. Mesoporous Anatase TiO₂ Beads with High Surface Areas and Controllable Pore Sizes: A Superior Candidate for High-Performance Dye-Sensitized Solar Cells. *Adv. Mater.* **2009**, *21*, 2206–2210.
- (11) Sauvage, F.; Chen, D. H.; Comte, P.; Huang, F. Z.; Cheng, Y. B.; Caruso, R. A.; Grätzel, M. Dye-Sensitized Solar Cells Employing a Single Film of Mesoporous TiO₂ Beads Achieve Power Conversion Efficiencies Over 10%. *ACS Nano* **2010**, *4*, 4420–4425.
- (12) Chen, D. H.; Cao, L.; Huang, F. Z.; Imperia, P.; Cheng, Y. B.; Caruso, R. A. Synthesis of Monodisperse Mesoporous Titania Beads with Controllable Diameter, High Surface Areas, and Variable Pore Diameters (14–23 nm). *J. Am. Chem. Soc.* **2010**, *132*, 4438–4444.
- (13) Yang, W. G.; Li, J. M.; Wang, Y.; Zhu, F.; Shi, W.; Wan, F. R.; Xu, D. S. A facile synthesis of anatase TiO₂ nanosheets-based hierarchical spheres with over 90% {001} facets for dye-sensitized solar cells. *Chem. Commun.* **2011**, *47*, 1809–1811.
- (14) Lee, J. C.; Kim, T. G.; Lee, W.; Han, S. H.; Sung, Y. M. Growth of CdS Nanorod-Coated TiO₂ Nanowires on Conductive Glass for Photovoltaic Applications. *Cryst. Growth Des.* **2009**, *9*, 4519–4523.
- (15) Kuang, D.; Brillet, J.; Chen, P.; Takata, M.; Uchida, S.; Miura, H.; Grätzel, M. Application of Highly Ordered TiO₂ Nanotube-Arrays in Flexible Dye-sensitized Solar Cells. *ACS Nano* **2008**, *2*, 1113–1116.
- (16) Mor, G. K.; Basham, J.; Paulose, M.; Kim, S.; Varghese, O. K.; Vaish, A.; Grimes, C. A. High-efficiency forster resonance energy transfer in solid-state dye sensitized solar cells. *Nano Lett.* **2010**, *10*, 2387–2394.
- (17) Chen, Q. W.; Xu, D. S. Large-scale, noncurling, and free-standing crystallized TiO₂ nanotube arrays for dye-sensitized solar cells. *J. Phys. Chem. C* **2009**, *113*, 6310–6314.
- (18) Chen, Q. W.; Xu, D. S.; Wu, Z. Y.; Liu, Z. F. Free-standing TiO₂ nanotube arrays made by anodic oxidation and ultrasonic splitting. *Nanotechnology* **2008**, *19*, 365708–365713.
- (19) Grätzel, M. Recent advances in sensitized mesoscopic solar cells. *Acc. Chem. Res.* **2009**, *42*, 1788–1798.
- (20) Dai, H.; Zhou, Y.; Chen, L.; Guo, B. L.; Li, A. D.; Yu, T.; Zou, Z. G. Porous ZnO nanosheet arrays constructed on weaved metal wire for flexible dye-sensitized solar cells. *Nanoscale* **2013**, *5*, 5102–5108.
- (21) Wang, Y. Q.; Chen, S. G.; Tang, X. H.; Palchik, O.; Zaban, A.; Kolytyn, Y.; Gedanken, A. Mesoporous titanium dioxide: sonochemical synthesis and application in dye-sensitized solar cells. *J. Mater. Chem.* **2001**, *11*, 521–526.
- (22) Wei, M. D.; Konishi, Y.; Zhou, H. S.; Yanagida, M.; Sugihara, H.; Arakawa, H. Highly efficient dye-sensitized solar cells composed of mesoporous titanium dioxide. *J. Mater. Chem.* **2006**, *16*, 1287–1293.
- (23) Koo, H. J.; Kim, Y. J.; Lee, Y. H.; Lee, W. I.; Kim, K.; Park, N. G. Nano-embossed hollow spherical TiO₂ as bifunctional material for high-efficiency dye-sensitized solar cells. *Adv. Mater.* **2008**, *20*, 195–199.
- (24) He, C. X.; Lei, B. X.; Wang, Y. F.; Su, C. Y.; Fang, Y. P.; Kuang, D. B. Sonochemical preparation of hierarchical ZnO hollow spheres for efficient dye-sensitized solar cells. *Chem.—Eur. J.* **2010**, *16*, 8757–8761.
- (25) Zhang, Q. F.; Chou, T. R.; Russo, B.; Jenekhe, S. A.; Cao, G. Z. Aggregation of ZnO nanocrystallites for high conversion efficiency in dye-sensitized solar cells. *Angew. Chem., Int. Ed.* **2008**, *47*, 2402–2406.
- (26) Wang, Y. F.; Li, J. W.; Hou, Y. F.; Yu, X. Y.; Su, C. Y.; Kuang, D. B. Hierarchical Tin Oxide Octahedra for Highly Efficient Dye-sensitized Solar Cells. *Chem.—Eur. J.* **2010**, *16*, 8620–8625.
- (27) Qian, J. F.; Liu, P.; Xiao, Y.; Jiang, Y.; Cao, Y. L.; Ai, X. P.; Yang, H. X. TiO₂-coated multilayered SnO₂ hollow microspheres for dye-sensitized solar cells. *Adv. Mater.* **2009**, *21*, 3663–3667.
- (28) Sun, Y. G.; Gates, B.; Mayers, B.; Xia, Y. N. Crystalline silver nanowires by soft solution processing. *Nano Lett.* **2002**, *2*, 165–168.
- (29) Yang, L.; Lin, Y.; Jia, J. G.; Xiao, X. R.; Li, X. P.; Zhou, X. W. Light harvesting enhancement for dye-sensitized solar cells by novel anode containing cauliflower-like TiO₂ spheres. *J. Power Sources* **2008**, *182*, 370–376.
- (30) Wang, Y. F.; Li, J. W.; Hou, Y. F.; Yu, X. Y.; Su, C. Y.; Kuang, D. B. Hierarchical tin oxide octahedral for highly efficient dye-sensitized solar cells. *Chem.—Eur. J.* **2010**, *16*, 8620–8625.
- (31) Qiu, Y. C.; Chen, W.; Yang, S. H. Facile hydrothermal preparation of hierarchically assembled, porous singlecrystalline ZnO nanoplates and their application in dye-sensitized solar cells. *J. Mater. Chem.* **2010**, *20*, 1001–1006.
- (32) Liao, J. Y.; Lei, B. X.; Kuang, D. B.; Su, C. Y. Tri-functional hierarchical TiO₂ spheres consisting of anatase nanorods and nanoparticles for high efficiency dye-sensitized solar cells. *Energy Environ. Sci.* **2011**, *4*, 4079–4085.
- (33) Wu, X.; Lu, G. Q.; Wang, L. Z. Shell-in-shell TiO₂ hollow sphere synthesized by one-pot hydrothermal method for dye-sensitized solar cell application. *Energy Environ. Sci.* **2011**, *4*, 3565–3572.
- (34) Kondo, Y.; Yoshikawa, H.; Awaga, K.; Murayama, M.; Mori, T.; Bandow, S.; Iijima, S. Preparation, Photocatalytic Activities, and Dye-Sensitized Solar-Cell Performance of Submicron-Scale TiO₂ Hollow Spheres. *Langmuir* **2007**, *24*, 547–550.
- (35) He, C. X.; Lei, B. X.; Wang, Y. F.; Su, C. Y.; Fang, Y. P.; Kuang, D. B. Sonochemical preparation of hierarchical ZnO hollow spheres for efficient dye-sensitized solar cells. *Chem.—Eur. J.* **2010**, *16*, 8757–8761.
- (36) Hore, S.; Vetter, C.; Kern, R.; Smit, H.; Hinsch, A. Influence of scattering layers on efficiency of dye-sensitized solar cells. *Sol. Energy Mater. Sol. Cells* **2006**, *90*, 1176–1188.
- (37) Wang, Y. F.; Li, J. W.; Hou, Y. F.; Yu, X. Y.; Su, C. Y.; Kuang, D. B. Hierarchical Tin Oxide Octahedra for Highly Efficient Dye-sensitized Solar Cells. *Chem.—Eur. J.* **2010**, *16*, 8620–8625.
- (38) Fisher, A. C.; Peter, L. M.; Ponomarev, E. A.; Walker, A. B.; Wijayantha, K. G. U. Intensity Dependence of the Back Reaction and Transport of Electrons in Dye-Sensitized Nanocrystalline TiO₂ Solar Cells. *J. Phys. Chem. B* **2000**, *104*, 949–958.
- (39) Bisquert, J. Diffusion Impedance and Space Charge Capacitance in the Nanoporous Dye-Sensitized Electrochemical Solar Cell. *J. Phys. Chem. B* **2003**, *107*, 13541–13543.
- (40) Hoshikawa, T.; Yamada, M.; Kikuchi, R.; Eguchi, K. Impedance analysis for dye-sensitized solar cells with a three-electrode system. *J. Electroanal. Chem.* **2005**, *577*, 339–348.
- (41) Bisquert, J.; Fabregat-Santiago, F.; Mora-Seró, I.; Garcia-Belmonte, G.; Giménez, S. Electron Lifetime in Dye-Sensitized Solar Cells: Theory and Interpretation of Measurements. *J. Phys. Chem. C* **2009**, *113*, 17278–17290.
- (42) Schlichterl, G.; Huang, S. Y.; Sprague, J.; Frank, A. J. Evaluation of the charge-collection efficiency of dye-sensitized nanocrystalline TiO₂ solar cells. *J. Phys. Chem. B* **1997**, *101*, 8141–8155.
- (43) Zhang, X.; Thavasi, V.; Mhaisalkar, S. G.; Ramakrishna, S. Novel hollow mesoporous 1D TiO₂ nanofibers as photovoltaic and photocatalytic materials. *Nanoscale* **2012**, *4*, 1707–1716.
- (44) Wang, Q.; Zhang, Z.; Zakeeruddin, S. M.; Grätzel, M. Enhancement of the performance of dye-sensitized solar cell by formation of shallow transport levels under visible light illumination. *J. Phys. Chem. C* **2008**, *112*, 7084–7092.
- (45) Frank, A. J.; Kopidakis, N.; Van de Lagemaat, J. Electrons in nanostructured TiO₂ solar cells: transport, recombination and photovoltaic properties. *Coord. Chem. Rev.* **2004**, *248*, 1165–1179.
- (46) Yuan, W.; Zhao, H.; Hu, H. Y.; Wang, S.; Baker, G. L. Synthesis and Characterization of the Hole-Conducting Silica/Polymer Nanocomposites and Application in Solid-State Dye-Sensitized Solar Cell. *ACS Appl. Mater. Interfaces* **2013**, *5*, 4155–4161.